WAMDII: wide-angle Michelson Doppler imaging interferometer for Spacelab

Gordon G. Shepherd, William A. Gault, D. W. Miller, Z. Pasturczyk, Sean F. Johnston, P. R. Kosteniuk, J. W. Haslett, David J. W. Kendall, and J. R. Wimperis

A wide-angle Michelson Doppler imaging interferometer (WAMDII) is described that is intended to measure upper atmospheric winds and temperatures from naturally occurring visible region emissions, using Spacelab as a platform. It is an achromatic field-widened instrument, with good thermal stability, that employs four quarterwave phase-stepped images to generate full images of velocity, temperature, and emission rate. For an apparent emission rate of 5 kR and binning into 85 × 105 pixels, the required exposure time is 1 sec. The concept and underlying principles are described, along with some fabrication details for the prototype instrument. The results of laboratory tests and field measurements using auroral emissions are described and discussed.

I. Introduction

WAMDII is a Spacelab instrument being developed to acquire images of winds and temperatures in the upper atmosphere. It employs the natural airglow and auroral visible emission lines as sources and derives line-of-sight velocities from the line shifts and temperatures from the linewidths. It is basically a Michelson interferometer with an imaging detector but with some special characteristics that optimize it for this purpose.

The primary characteristic is that of field widening. The principle of compensating a Michelson interferometer (hereinafter referred to as an MI) was first described by Hansen[1] and Hansen and Kinder.[2] Evans[3] proposed its use as an alternative to the birefringent photometer. The application to Fourier transform spectroscopy was suggested by Mertz[4] who developed the concept in subsequent publications.[5,6] The first practical version was described by Bouchareine and Connes.[7] Steel[8] has given an interesting description of the field-widened MI, characterizing it as a configuration that introduces delay without shift. An excellent review of these developments has been given by Baker.[9] A field-widened interferometer has an optical path difference that varies slowly with incident angle; this allows the collection of light over a large solid angle onto the detector, providing a large sensitivity. Hilliard and Shepherd[10] showed that the gain over a conventional Michelson interferometer is $2n\sqrt{R}$, where R is the resolving power, and n is the refractive index of the field-widening medium. In previous applications this gain was the reason for using field widening. Here we use the large solid angle in a different way, for imaging. The sensitivity advantage is then lost, in terms of a single pixel, but the total information yield can be enormously increased. In this context the purpose of field widening is to permit the use of an imaging detector with interferometer phase variations that are small over the field of view, only a fraction of a wavelength over off-axis angles of 6° or so.

Field widening a scanning MI over a large path difference is a challenging problem.[9,11] The only really successful and widely used instruments are those developed at Utah State University.[12] However, these instruments do not achieve resolutions sufficient to measure linewidths or shifts. Hilliard and Shepherd[10] devised a simple implementation that was capable of measuring the widths of single lines of known shape, such as the forbidden upper atmospheric emissions OI 557.7 nm and OI 630 nm which in general have purely thermal line shapes. A Gaussian line shape results in a Gaussian interferogram, so that monitoring the fringe

G. G. Shepherd and W. A. Gault are with York University, Centre for Research in Experimental Space Science, Toronto M3J 1P3; D. W. Miller and Z. Pasturczyk are with SED Systems, Inc., Saskatoon S7K 3P7; S. F. Johnston is with Bomem, Inc., Vanier, Quebec G1M 2Y2; P. R. Kostiuk is with University of Saskatchewan, Physics Department, Saskatoon S7N 0W0; J. W. Haslett is with University of Calgary, Department of Electrical Engineering, Calgary T2N 1N4; D. J. W. Kendall is with National Research Council of Canada, Canada Centre for Space Science, Ottawa K1A 0R6; and J. R. Wimperis is with Interoptics, Ltd., Ottawa K2G 0G3.

Received 19 July 1984.
0003-6935/85/111571-14$02.00/0.

modulation depth at one path difference allows the linewidth to be inferred. This approach was applied by Hilliard and Shepherd[13] and Zwick and Shepherd[14] to the measurement of upper atmospheric temperatures, with some success. More recently, it was recognized that the same concept would apply to the measurement of winds.

At an essentially fixed path difference, the device records a single fringe, whose modulation depth depends solely on the width of the source emission line and whose phase depends on the wavelength shift or wind velocity. The problem is then to measure the modulation depth and the phase for each pixel in the image. This is done by stepping the interferometer optical path difference in quarterwave steps. Three measurements are sufficient to determine three quantities, the mean value, the fringe amplitude, and the fringe phase. By combining the three signal values for a given pixel, the wind, temperature, and emission line intensity are deduced. This is repeated for the whole image, yielding images of wind, temperature, and intensity. This method of using an imaging detector is different from the way focal plane detectors have been used with Fabry-Perot interferometers.[15–17] It provides true imaging in the sense that the wind, temperature, and intensity are measured for every pixel for which sufficient emission intensity is present.

Preliminary descriptions of the instrument have been given.[18,19] In the sections following, we describe the basic theory and concept as implemented in the WAMDII. After describing some aspects of the fabrication the results of laboratory tests of a system prototype are described and finally some field measurements are presented.

II. Derivation of Wind and Temperature

The auroral and airglow OI 557.7- and 630.0-nm emission lines are forbidden transitions arising from the $1S$ and $1D$ levels, respectively, with respective radiative lifetimes of 0.9 and 147 sec. In general, oxygen atoms in these metastable states collide with their neighbors several times before radiating, so that they are in thermal equilibrium. There are exceptions, especially for the 557.7-nm line,[20] but in general one can assume that these lines are Gaussian. They are also single lines, because there are no isotopic effects and oxygen has zero nuclear spin. With suitable prefilters, single lines can be isolated in molecular bands, although often these are doublets, in which case the interferometer path difference must be chosen to put the two components in phase.

For a single Gaussian line, the spectrum is given by

$$B(\sigma) = B_0 \exp[-4 \ln 2(\sigma - \sigma_0)^2/w^2], \quad (1)$$

where σ is the wave number in the spectrum, σ_0 is the wave number of the line center, and w is the full width at half-intensity (all in cm^{-1}). The interferogram of the line presented by a Michelson interferometer is given by the Fourier transform of Eq. (1):

$$I(\Delta) = I_0[1 + \exp(-QT\Delta^2) \cos 2\pi\sigma_0\Delta], \quad (2)$$

where Δ = optical path difference in cm, T = temperature in K, and where $Q = 1.82 \times 10^{-12}(\sigma_0^2/M)$ K^{-1} cm^{-2}, in which M is atomic mass. The exponential term can be regarded as the fringe visibility, as originally defined by Michelson:

$$V = \exp(-QT\Delta^2) = (I_{max} - I_{min})/(I_{max} + I_{min}). \quad (3)$$

The basic interferogram equation for the WAMDII can thus be written as

$$I = I_0[1 + V \cos(2\pi\sigma_0\Delta)]. \quad (4)$$

If σ_0 corresponds to the wave number for zero wind velocity, we can write

$$\sigma = \sigma_0(1 + v/c), \quad (5)$$

where v is the line-of-sight velocity of the source and c is the velocity of light. If we now define $\Delta = \Delta_0 + \Delta'$ and arbitrarily choose Δ_0 so that $\cos 2\pi\sigma_0\Delta_0 = 1$, neglecting the term in $v\Delta'/c$ we have

$$I = I_0[1 + V \cos(2\pi\sigma_0\Delta' + \phi)], \quad (6)$$

where

$$\phi = 2\pi\sigma_0\Delta_0 v/c. \quad (7)$$

For a wavelength of 500 nm and an optical path difference of 5 cm, $\phi = 0.12\ v$ deg, where v is in m/sec. To measure winds as small as 10 m/sec, we must be able to detect phase shifts of 1.2°.

Now a simple way to measure v, ϕ, and I_0 is required. Suppose that we increment Δ' in steps of $\lambda/4$ from $\Delta' = 0$, taking four settings altogether. We then obtain from Eq. (6) for the intensities measured at each of the steps:

$$I_1 = I_0(1 + V \cos\phi), \quad (8)$$

$$I_2 = I_0(1 - V \sin\phi), \quad (9)$$

$$I_3 = I_0(1 - V \cos\phi), \quad (10)$$

$$I_4 = I_0(1 + V \sin\phi). \quad (11)$$

From these equations one can find that

$$I_0 = (I_1 + I_3)/2 = (I_2 + I_4)/2, \quad (12)$$

$$V = [(I_1 - I_3)^2 + (I_4 - I_2)^2]^{1/2}/2I_0, \quad (13)$$

$$\tan\phi = (I_4 - I_2)/(I_1 - I_3). \quad (14)$$

As stated in Sec. I, only three signal values are actually required. However, the above equations have an attractive symmetrical form, and Eq. (12) allows one to test for intensity variations during the image sequence which may then be corrected for systematic trends. For example, in the present instrument the two values of I_0 were found to be not precisely equal, owing to weak extraneous fringes for which it was necessary to correct (discussed in Sec. VII.C).

Equation (14) has the highly desirable virtue that, where the same pixel is used for all four measurements, the dark levels and the gains cancel, so that there is no dependence whatever on system calibration. For Eq. (13) there is a dark level dependence but no gain dependence. This is extremely important in an imaging situation where one would otherwise have to keep track

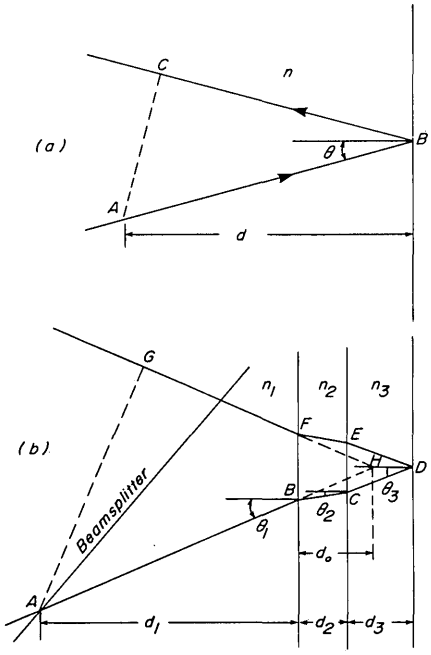

Fig. 1. (a) Generalized optical path difference ABC through a plate of refractive index n and thickness d. (b) Generalized path difference for three glass plates of thicknesses d_1, d_2, and d_3 and refractive indices n_1, n_2, and n_3, respectively.

of 9010 dark levels and gains and their continuing calibration and interpolation during the mission.

III. Interferometer Path Difference Equation

A. Generalized Path Length

Figure 1(a) shows a ray passing through a plate of refractive index n and reflecting from the back at incident angle θ. The optical path length P, from an arbitrary point A to the reflection at B and back to C, the foot of the normal drawn through A, is given by

$$P = 2nd\cos\theta. \tag{15}$$

This can be generalized to three plane-parallel plates, as shown in Fig. 1(b). The ray travels the path $ABCDEFG$, where now G is the foot of the normal through the arbitrary point A. The intersection of AB and GF projected is at H. The optical path length from A to G is $n_1(AHG–BHF) + 2n_2BC + 2n_3CD$, so that

$$P = 2n_1(d_1 + d_0)\cos\theta_1 - \frac{2n_1d_0}{\cos\theta_1} + \frac{2n_2d_2}{\cos\theta_2} + \frac{2n_3d_3}{\cos\theta_3}. \tag{16}$$

It can be seen that

$$d_0\tan\theta_1 = d_2\tan\theta_2 + d_3\tan\theta_3, \tag{17}$$

and applying Snell's law,

$$d_0/(n_1\cos\theta_1) = d_2/(n_2\cos\theta_2) + d_3/(n_3\cos\theta_3). \tag{18}$$

This can be substituted into Eq. (16), which after some manipulation gives

$$P = 2n_1d_1\cos\theta_1 + 2n_2d_2\cos\theta_2 + 2n_3d_3\cos\theta_3. \tag{19}$$

This expression can be further generalized to any number of plates. Note that in Fig. 1(b) a beam splitting layer has been added, at an arbitrary angle, so that A is defined by the intersection of the ray with this layer. This has no effect on the path length equation but is needed to introduce the next section.

B. Field Widening

We will specify from this point on an interferometer consisting of a symmetrical beam splitter and two arms, one arm containing some beam splitter material (d_1,n_1) and two plates (d_2,n_2), (d_3,n_3), while the other arm contains some beam splitter material (d_1',n_1') and one plate (d_2',n_2'). The path difference is then

$$\begin{aligned}\Delta &= P - P' \\ &= 2n_1d_1\cos\theta_1 - 2n_1'd_1'\cos\theta_1' + 2n_2d_2\cos\theta_2 \\ &\quad - 2n_2'd_2'\cos\theta_2' + 2n_3d_3\cos\theta_3.\end{aligned} \tag{20}$$

For a symmetrical beam splitter the first two terms disappear, and we simplify our notation by setting $n_2' = n_1$, $d_2' = d_1$, to write

$$\Delta = 2(n_3d_3\cos\theta_3 + n_2d_2\cos\theta_2 - n_1d_1\cos\theta_1). \tag{21}$$

Rewriting this equation in terms of the angle incident in air on the beam splitter, denoted i, one obtains

$$\begin{aligned}\Delta = 2[&n_3d_3(1 - \sin^2i/n_3^2)^{1/2} + n_2d_2(1 - \sin^2i/n_2^2)^{1/2} \\ &- n_1d_1(1 - \sin^2i/n_1^2)^{1/2}].\end{aligned} \tag{22}$$

This can be expanded to fourth order, yielding

$$\begin{aligned}\Delta/2 = {}& n_3d_3 + n_2d_2 - n_1d_1 \\ &- \frac{\sin^2i}{2}\left(\frac{d_3}{n_3} + \frac{d_2}{n_2} - \frac{d_1}{n_1}\right) - \frac{\sin^4i}{8}\left(\frac{d_3}{n_3^3} + \frac{d_2}{n_2^3} - \frac{d_1}{n_1^3}\right)\end{aligned} \tag{23}$$

Field widening is accomplished by setting the second-order term equal to zero, which requires that

$$d_3/n_3 + d_2/n_2 - d_1/n_1 = 0. \tag{24}$$

The path difference is then independent of incident angle to fourth order.

C. Chromatic Compensation

Because of the dependence of refractive index on wavelength, the wide-angle condition (24) can be strictly maintained at only one wavelength. Title and Ramsey[21] have shown how the arm materials can be chosen to provide some degree of achromaticity. Let the departure from the wide-angle condition be w. Then

$$w = d_3/n_3 + d_2/n_2 - d_1/n_1. \tag{25}$$

Taking the derivative with respect to wavelength,

$$\frac{dw}{d\lambda} = -\frac{d_3}{n_3^2}\frac{dn_3}{d\lambda} - \frac{d_2}{n_2^2}\frac{dn_2}{d\lambda} + \frac{d_1}{n_1^2}\frac{dn_1}{d\lambda}. \tag{26}$$

For the WAMDII, d_3 is a thin vacuum gap, so that the refractive index is independent of wavelength; to obtain $dw/d\lambda = 0$ here requires

$$(d_2/n_2^2)(dn_2/d\lambda) = (d_1/n_1^2)(dn_1/d\lambda). \tag{27}$$

For the case where the vacuum gap has zero thickness, substitution of the wide-angle condition (24) reduces this equation to the two-glass case given by Title and Ramsey[21]:

$$(1/n_1)dn_1/d\lambda = (1/n_2)dn_2/d\lambda. \quad (28)$$

In this case the interferometer can be made achromatic by selecting two glasses of equal $(1/n)dn/d\lambda$, quite independently of the arm lengths. But suppose that the two quantities are not precisely equal, so that

$$(1/n_1)dn_1/d\lambda - (1/n_2)dn_2/d\lambda = p. \quad (29)$$

We now reintroduce the finite vacuum gap and apply the wide-angle condition (24) and the chromatic condition (27) to obtain

$$d_3/d_1 = -(n_2/n_1)[p/(dn_2/d\lambda)]. \quad (30)$$

We see that a small mismatching of the two glasses, p, can be accommodated by a small vacuum gap d_3.

D. Thermal Compensation

To be useful for Doppler line shift measurements, the path difference must be stable. A wind error of 10 m/sec corresponds to a measurement of one part in 3×10^7. Thermal expansion coefficients for glass are $\sim 5 \times 10^{-6}°C^{-1}$, or one part in 2×10^5 for 1°C, implying a thermal stability requirement of 0.01°C. Using quartz does not help all that much, because the effect of the refractive-index change with temperature is comparable with that for glass. Values of $(1/n)(dn/dT)$ for glass are $\sim 2 \times 10^{-6}°C^{-1}$.

In the WAMDII the thickness of the vacuum gap is controlled by a servo system that senses the capacitance of a small gap within the cavity, so that this thickness and its refractive index are immune to temperature change. The variation of the path difference with temperature thus depends only on the other two glasses:

$$d\Delta_0/dT = 2(n_2\delta d_2/\delta T + d_2\delta n_2/\delta T - n_1\delta d_1/\delta T - d_1\delta n_1/\delta T). \quad (31)$$

Applying the wide-angle condition (24) for two glasses (again temporarily setting the vacuum gap to zero) the above can be written

$$\frac{d\Delta_0}{dT} = 2n_1d_1\left[\left(\frac{n_2}{n_1}\right)^2\left(\frac{1\delta d_2}{d_2\delta T} + \frac{1\delta n_2}{n_2\delta T}\right) - \left(\frac{1\delta d_1}{d_1\delta T} + \frac{1\delta n_1}{n_1\delta T}\right)\right], \quad (32)$$

which can be set equal to zero by having

$$n_1^2\left(\frac{1\delta d_1}{d_1\delta T} + \frac{1\delta n_1}{n_1\delta T}\right) = n_2^2\left(\frac{1\delta d_2}{d_2\delta T} + \frac{1\delta n_2}{n_2\delta T}\right). \quad (33)$$

Since $(1/d)\delta d/\delta T$ is the linear expansion coefficient, it is clear that the thermal condition (33) is independent of arm lengths, as shown by Title and Ramsey,[21] who also demonstrated that a number of pairs of glasses exist that simultaneously closely satisfy the chromatic requirement (28) and this thermal requirement (33).

E. Choice of Configuration

The objective was to construct a field-widened achromatic thermally compensated Michelson interferometer using two-arm glasses. However, to scan over one fringe a thin vacuum gap was required as well, which makes an extra degree of freedom available. Twenty-six candidate glass pairs were examined with regard to meeting the criteria defined by Eqs. (28) and (33), as well as for glass availability, and LF5 and LaF21 were selected. The values for these glasses are given in Table I. The lengths d_1 and d_2 are then approximately fixed by the path difference Eq. (21) and the field-widening Eq. (24).

Since the thermal equation for two glasses [Eq. (33)] may not be exactly satisfied by the selected materials, we can return to Eq. (31) and set $d\Delta/dT = 0$ by the requirement that

$$d_2(n_2\alpha_2 + \beta_2) = d_1(n_1\alpha_1 + \beta_1) \text{ where } \beta = dn/dT. \quad (34)$$

Table I. Properties of the WAMDII Arm Glasses

Linear expansion coefficient, α		Schott LaF21 5.9×10^{-6} K^{-1}	Ohara LF5 8.7×10^{-6} K^{-1}
Coefficients of dispersion formula[a] for wavelength λ in microns	A_0	3.122280	2.447787
	A_1	-1.3500×10^{-2}	-1.0000×10^{-2}
	A_2	2.5833167×10^{-2}	1.7531120×10^{-2}
	A_3	5.8672351×10^{-4}	9.5250889×10^{-4}
	A_4	$-7.0659294 \times 10^{-6}$	$-5.4837761 \times 10^{-5}$
	A_5	1.5283898×10^{-6}	4.7303899×10^{-6}
$\Delta n/\Delta T$ *absolute* $(10^{-6}/K^{-1})$:			
$T = 20°C$, $\lambda = 5577$ Å		3.16	1.73
$\lambda = 6300$ Å		2.90	1.28
$\lambda = 7620$ Å		2.59	0.47
$T = 25°C$, $\lambda = 5577$ Å		3.21	1.83
$\lambda = 6300$ Å		2.97	1.38
$\lambda = 7620$ Å		2.66	0.57
$T = 30°C$, $\lambda = 5577$ Å		3.26	1.93
$\lambda = 6300$ Å		3.04	1.48
$\lambda = 7620$ Å		2.72	0.67

[a] Dispersion formula at 25°C, $n^2 = A_0 + A_1\lambda^2 + A_2\lambda^{-2} + A_3\lambda^{-4} + A_4\lambda^{-6} + A_5\lambda^{-8}$.

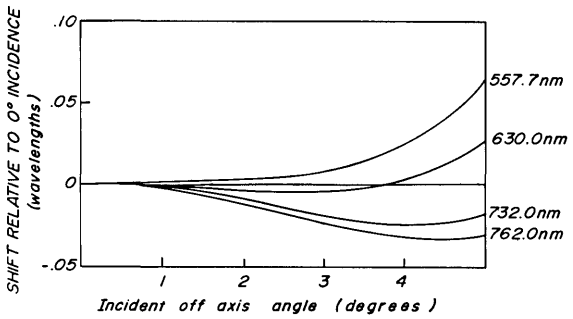

Fig. 2. Calculated variation of optical path difference (OPD) relative to the value at normal incidence for four candidate wavelengths for use in the WAMDII. The model is for an LF5 thickness of 5.36908 cm, an LaF21 thickness of 6.00122 cm, and a vacuum gap in the LaF21 arm of 0.0382-cm thickness. The glass constants are from Table I.

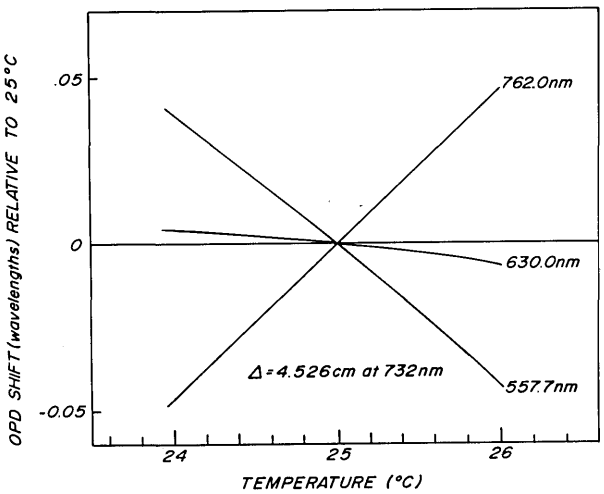

Fig. 3. Calculated variation of OPD relative to the value at 25°C as a function of temperature for three wavelengths. The model is the same as for Fig. 2.

The ratio d_2:d_1 can be precisely set to meet this condition for thermal compensation. d_3 can now be chosen either to satisfy the achromaticity condition (29) or the field-widening condition (24). It is not difficult to approximately satisfy both where the gap is small, as there is considerable margin in the field-widening condition. In fact, Zwick and Shepherd[22] have shown that, when the error is in the right direction, the field widening can be improved by defocusing, where in Eq. (22) the second-order term is balanced off against the fourth-order term. The final solution for an optical path difference of 4.526 cm at 732 nm (or 4.563 cm at 546 nm) was found through numerical modeling of the conditions near those described above, and the results are shown in Fig. 2, where the path difference as a function of incident angle is shown for the wavelengths to be used in the WAMDII mission. In Fig. 3, the variation of path difference with temperature is shown as a function of temperature for these same wavelengths.

The variation of path difference with incident angle is well within the limits required. The calculated thermal variation is excellent for the design wavelength and is acceptable for the other wavelengths.

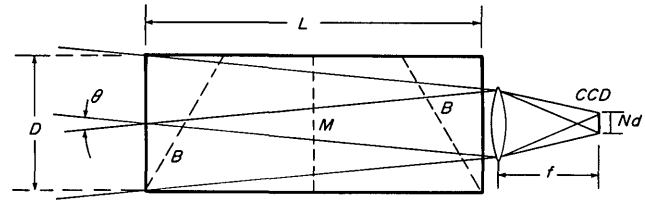

Fig. 4. One geometrical configuration for imaging through an unfolded Michelson interferometer; the camera lens is the aperture stop. B indicates the beam splitter (which is traversed twice) and M denotes the mirror.

IV. System Responsivity

By responsivity we mean the ratio of the output signal to the input source radiance. One of the paradoxical features of a long-path field-widened Michelson interferometer is that its usable responsivity is not limited by the field-widening characteristic but simply by the geometry involved in getting light through a block of glass; this section is concerned with the optimization of that situation.

The simplest configuration for the WAMDII would be as shown in Fig. 4. Here we draw the MI as a box of length L and cross section D. To simplify matters we let L be the air-equivalent length so that we need not consider refraction at the boundaries. The mirrors are located at the center of the box, and there are two effective beam splitters, one on each side. However they play no role here and may be ignored.

The photon flux collected by a pixel is given by

$$A\Omega = y^2\theta^2/N^2, \tag{35}$$

where y is the dimension of the square lens, θ is the full angle of the field of view, and N is the number of pixels along one side of the CCD. But the lens size is determined by

$$y = D - \theta L. \tag{36}$$

Therefore we can write

$$A\Omega = (\theta^2N^2)(D - \theta L)^2. \tag{37}$$

As the field of view increases the solid angle term (the first one) increases, but the size of the aperture stop (the second term) decreases. There is a maximum for $\theta = D/2L$ (we use the small-angle approximation throughout this section for simplicity) and that maximum value is given by

$$A\Omega = D^4/(16N^2L^2). \tag{38}$$

This configuration has a severe practical limitation, which is that of scattered light inside the system, owing to the lack of stops. A useful system also requires telescopic input optics to permit the external field of view to be changed, and the introduction of field and aperture stops.

For the WAMDII the alternative configuration of Fig. 5 is used. S_1 is a field stop that controls the field of view in front, and it is imaged on the CCD. S_2 is an aperture stop located on the mirrors, and it is imaged on L_1. The field of view in front can now be determined indepen-

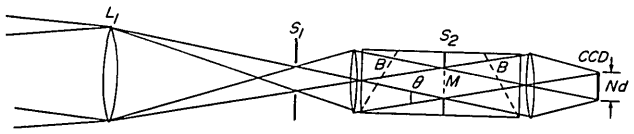

Fig. 5. The WAMDII configuration: the aperture stop S_2 is located on the Michelson mirrors, and a field stop S_1 is introduced in front of the *MI*.

dently of the angle inside the MI. The stop S_2 now plays the role of the camera lens in the first configuration, so that the appropriate equation is

$$A\Omega = (\theta^2/N^2)(D - \theta L/2)^2, \tag{39}$$

which has a maximum value for $\theta = D/L$, giving

$$A\Omega = D^4/(4N^2L^2). \tag{40}$$

Thus the latter system has the better responsivity and so is superior in all respects. The D^4 dependence shows how critical is the size of the MI. We therefore set out to manufacture the largest set of optics that was thought to be feasible, with a face size of 8.89 cm, giving a clear diameter of 7.6 cm. L is determined by factors discussed in the previous section, all of which are fixed by independent considerations; it is equal to 27 cm. This leaves N as the only free parameter. For the WAMDII it is possible to control the responsivity by on-chip averaging, with a further possibility of reduction of N in the data processing.

All this is satisfyingly simple but we must now face some practical considerations in the selection of the camera lens and the CCD. These are related through $\theta_{max} = W/f = D/L$ where W is the linear dimension of the CCD and f is the camera focal length. The largest CCD available to us has dimensions of 9.75 × 7.31 mm, which immediately fixed the lens focal length at 3.45 cm. But this lens must fill the output face of the MI, giving an f/No. equal to 0.45. This presents a challenge, but we note that the output face is not a stop and so this is only an effective f/No. Assuming that this is possible, we can proceed to calculate the responsivity. If we set $N = 100$ we obtain $A\Omega = 1.2 \times 10^{-4}$ cm^2 sr and if we introduce a system transmission of 0.3 and quantum efficiency of 0.8 (an important virtue of the CCD), we find that the responsivity is 1.9 electrons/sec/R. That is, for a 1-kR aurora, the rate is 1900 electrons/sec and to accumulate the 10^4 electrons needed for 1% statistics we need an exposure time of 5 sec. For the full CCD the number of accumulated electrons is 10^8, a very large signal.

V. Choice of CCD Imager

A number of different solid-state area detector technologies were available at the time that the WAMDII was conceived. These can be broadly categorized into four types: photodiode, charge injection, interline transfer, and frame transfer devices.

Photodiode arrays have, until recently, consisted of a relatively small number of picture elements (pixels) and, although the arrays can be obtained blemish free, dead zones between cells coupled with low spatial resolution have made them less attractive than other types of charge-coupled device (CCD) array for scientific imaging.

Charge injection devices are based on a surface channel CCD technology where device topology is arranged to allow random access to a particular pixel during readout. The random access read feature is unique but not particularly useful to the WAMDII and the surface channel fabrication yields a noisy device which is unacceptable for this application.

An interline transfer CCD has columns of pixels interleaved with columns of transport registers which are usually opaque. Image integration takes place in the active pixels, and the resulting charge packets are transferred to the vertical transport registers for readout. At relatively slow readout rates, the transport registers must be opaque to prevent image smearing when a shutter system is not employed, which results in dead zones in a frontside illuminated device.

To obtain a fully active image area, the frame transfer technique is used. In this type of imager, separate image and storage areas are fabricated. The storage area is normally masked to facilitate slow readout rates without smearing. Once an image is integrated in the image area, it can be transferred at high speed to the storage area (again to prevent smearing) and read out at a slower rate compatible with signal chain circuit maximum speed limitations. Since frame transfer devices are available in buried channel technology (less noise) with large overall chip area and a large number of elements for high spatial resolution, this type of imager was chosen for the WAMDII.

Of the frame transfer devices readily available to us commercially, the RCA SID 52000 series of imagers and the English Electric EEV P8600 imagers are the most promising. Both devices have an acceptably large overall active image area of ~50 mm^2, an important consideration for the instrument. The RCA devices are thinned backside illuminated arrays, which result in a full active image area with no dead zones and a high quantum efficiency, typically >70% at effect, with low charge transfer efficiency (CTE) at low light levels. It is not clear whether this has been resolved in the current production devices. The EEV devices have lower quantum efficiency (40% typical at 550 nm) but are substantially cheaper (a factor of 5) and at present are more readily available. They do not appear to exhibit low level CTE degradation.

A number of device parameters have important implications for the successful operation of the WAMDII. In particular, dark current rates, readout noise, charge transfer efficiency, and quantum efficiency have an influence on overall system performance.

Dark current corresponds to the thermal generation rate of hole–electron pairs in the active image area of the CCD in the absence of incoming photon flux. Because of internal fields produced by the gate electrode voltages, electrons accumulate in the pixel potential wells, holes are swept into the substrate where they recombine, and a charge packet builds up in the pixel with time. It has been shown[23] that a good approximation

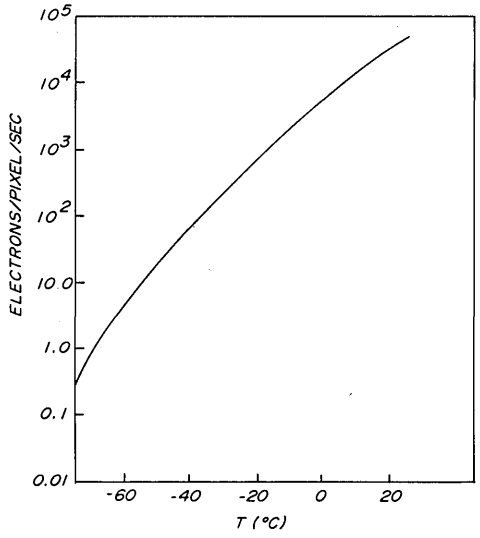

Fig. 6. Modeled dark electron rate for a theoretical RCA CCD based on a 30- × 30-μm active pixel size. The electron rate is normalized to a value of 1 nA/cm^2 at 300 K.

to the temperature dependence of dark current is given by

$$\frac{J_D}{J_D(300)} = AT^{3/2}\exp[-E_g(T)/2kT], \tag{41}$$

where

$$A = 3.644 \times 10^5\ \mathrm{K}^{-3/2},$$

$$J_D(300) = \text{dark rate at 300 K (nA/cm}^2\text{)}, \tag{42}$$

$$E_g(T) = 1.1557 - \frac{7.021 \times 10^{-4}T^2\ \mathrm{eV}}{(1108 + T)}.$$

This results in the curve shown in Fig. 6, which is normalized to 1 nA/cm^2 at 300 K. Good quality devices exhibit rates of 1–10 nA/cm^2 at 25°C, so that for the WAMDII, operation at −45°C with 5-sec integration times results in an accumulated dark charge of 100–1000 electrons/pixel. At the rate of 9500 electrons/pixel quoted in Sec. IV, this can represent an error of a few percent and must be taken into account, particularly when the visibility is calculated.

Noise is a second limitation which has implications for the satisfactory operation of the instrument. There are actually three major sources of noise within the imager; signal shot noise, reset noise, and readout noise. Signal shot noise occurs because of the random way in which hole–electron pairs are created as incoming photons interact with the silicon lattice, which results in an uncertainty in the actual size of a particular charge packet for a given integration time. It has been shown[24,25] that the uncertainty in a packet with mean value N electrons is $\sqrt{N}$ rms electrons. It then follows that, as a percentage of mean value, the uncertainty decreases as mean signal value increases. Thus as mentioned before, signal packets must exceed 10^4 electrons to achieve 1% statistics. It also suggests that reset noise and readout noise levels must be reduced well below the 100 rms electron level to achieve the desired performance. Reset noise results from the thermal noise of the reset transistor in the output stage, and it can be shown that

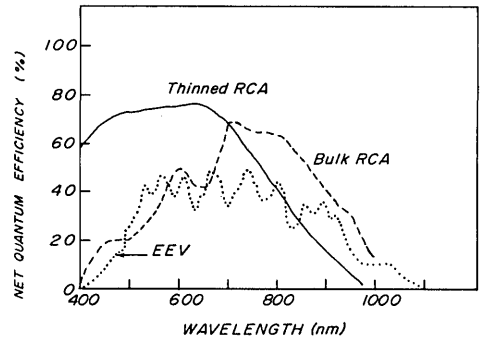

Fig. 7. Quantum efficiency vs wavelength for three different CCD devices.

$$N_{\mathrm{rms}}(\text{reset}) = 400\sqrt{C}\ (\mathrm{pF})\ \text{rms electrons}. \tag{43}$$

Typically $C = 0.013$ F for the imagers under consideration which gives a reset noise level of 145 electrons, well above the acceptable limit. Fortunately, reset noise can be largely removed by careful design of a correlated double sampling circuit, and it should be possible to reduce the noise level due to this mechanism well below 100 electrons. The final source of noise, readout noise, results from noise in the output transistor itself. The output transistor generally exhibits $1/f$ noise in the operating frequency range of interest. Typical measured input referred noise voltages for the EEV device are in the range from 100 to 300 nV/$\sqrt{\mathrm{Hz}}$ at 10 kHz. Values for the new RCA devices are not yet available but are expected to be similar. This noise component can be minimized by using a dual slope integrator circuit as a correlated double sampler in the signal chain. It is expected that by careful signal chain design, this noise component can be reduced to the 15–30 rms electron range at the clock rates planned for the WAMDII.

Quantum efficiency varies widely depending on device fabrication technology. The quantum efficiency parameter is a strong function of wavelength, peaking near the 650-nm wavelength region for both the RCA and EEV devices. Typical efficiency plots[26] for both devices are shown in Fig. 7. The bulk RCA and EEV devices are thick frontside illuminated arrays and effective quantum efficiency variations due to interference effects are readily apparent. The thinned backside illuminated RCA device, on the other hand, exhibits much improved response at shorter wavelengths and generally higher overall quantum efficiency at the wavelengths of interest. It is this aspect of RCA device performance which makes it the best choice for the WAMDII at present.

VI. Description of the Interferometer Optics

The MI proper consists of a solid cemented glass assembly. The largest component is a hexagonal beam splitter formed by cementing two BK7 prisms, one of which carries the beam splitting coating. This all-dielectric thin-film multilayer system has an efficiency of ~92% in the 550–750-nm spectral region, and it can

be used with an acceptance angle of up to 13° measured in air. Its design is described in greater detail in a companion paper.[27] To faces of the hexagon that are on opposite sides of the beam splitting layer are cemented arms of Schott LaF21 and Ohara LF5 glass. The other two optical faces of the beam splitter prism, namely, the entrance and exit faces, are antireflection coated to keep reflectance below 0.5% over most of the spectral range of 550–770 nm.

The end of the LF5 arm supports a deposited mirror comprising an aluminum layer over a dielectric stack. The LaF21 arm supports the scan mirror consisting of a quartz assembly actuated by piezoelectric transducers and employing several capacitors for position sensing. The scan mirror assembly is an adaptation of a commercial design utilized for Fabry-Perot interferometers.[28]

The free end of the LaF21 arm is antireflection coated and also supports deposited capacitor pads and reflective spots which served as small Fabry-Perot interferometers during testing of the scan assemby. The vacuum gap between the scan mirror and LaF21 arm is ~390 μm.

Design and fabrication of the interferometer optics presented several practical problems. The expressions given in Sec. III served as the basis of the design and for investigation of the required manufacturing tolerances. Glass homogeneity, surface flatness, and parallelness proved to be extremely critical. In addition, the reliability of the optical constants listed in Table I was crucial to the accurate specification of dimensions.

Glass homogeneity of the highest quality proved to be marginally sufficient for the path lengths and apertures involved in the WAMDII. The uncommon LaF21 glass, in particular, evinced a strong index gradient immediately outside the optical aperture.

Reflective surfaces of the MI were polished flat to better than $\lambda/25$ peak-to-peak over the optical aperture, while transmissive surfaces were typically polished to $\lambda/10$. The weak spherical figure of the various surfaces and an astigmatic distortion introduced by the LaF21 glass were corrected at the LF5 mirror prior to cementing the arm to the rest of the assembly.

Besides glass quality and surface flatness, the wave front distortion (and hence visibility of the final instrument) is dependent on the uniformity of the optical cement. The WAMDII employs cement in the optical aperture owing to the requirements of low stray light, strong relaxation-free joints, and wide temperature survivability. The choice of cements was finally restricted to Norland 61, with extreme care taken to assure uniform ultraviolet curing.[29]

Despite these influences, the wave front error of the completed MI proved to be $\lambda/10$ peak-to-peak, considerably better than the expected distortion.

VII. Laboratory Test Results

A. Laboratory Test Configuration

Extensive tests were performed to prove the instrument concept and to verify and characterize subsystem and system level performance parameters. The most significant results are described in this section and compared with theoretical predictions and design goals. Since the foreoptics illustrated in Fig. 5 were not fabricated in this phase, a special setup was required. The configuration shown in Fig. 8, which also shows the layout of the WAMDII instrument itself, consists of a large plano-convex lens (eyepiece) which images a small flat field source (objective) onto the MI mirror. The field stop is imaged on the CCD array. The monochromator resolution of ~1 nm is sufficient to select single emission lines from the spectrum emitted by the spectral lamp. Three electrodeless lamps filled with Hg, Ne, and Ar were used to cover the full spectral range of the WAMDII. The emission lines generated by this system were measured prior to the tests, using a long path scanning Michelson interferometer. The linewidths vary from 1 to 3 pm, resulting in visibilities, for the WAMDII optical path difference of 0.95–0.75, respectively. The emission lines were suitably intense for the measurement; their intensities were extremely stable, to within ±0.3%.

B. Scanning Mirror Step Size Calibration

Under computer control the scanning mirror mechanism described in Sec. VI can be scanned over a range of ~2 μm in quantized steps of ~0.5 nm. The first test provided an accurate calibration of this elemental step size. Based on an assumed elemental step of 0.5 nm, the

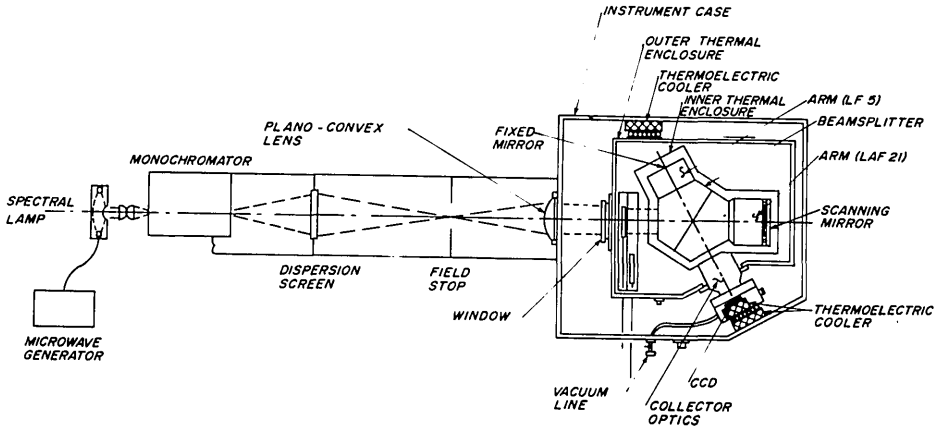

Fig. 8. The WAMDII developmental model and emission line source configuration used for laboratory tests.

Table II. Measured Instrument Visibility

Wavelength (nm)	Instrument visibility (corrected for linewidth)	
	Filter ⊥ to optical axis	No filter and tilted filter
546.07	0.72	0.79
692.95	0.71	0.82
763.51	0.78	0.90

interferogram of a neon line at 692.947 nm was scanned in λ/20 steps across two fringes. A sinusoid was least-squares fitted to the raw data of the 40 images for 500 pixels. The average ratio of the requested step size to the determined step size was used to refine the elemental step size. The procedure continued by iteration until the ratio of the requested to the returned step size was sufficiently close to unity. The elemental step size was thus determined to be 0.4246 nm. As a further check, the step size calibration was repeated at four other wavelengths from 546 to 764 nm and from 23.53°C to 26.08°C. The results were consistent and repeatable across the spectral range and were independent of temperature.

C. Visibility Measurements

It was expected that the instrument visibility would approach 0.9, based on the wave front error of the manufactured optics and the polarization effects of the beam splitter. The apparent visibility was determined by scanning the mirror in λ/40 steps of 1.5 fringes for several wavelengths covering the WAMDII spectral range. The apparent visibility was then divided by the emission line visibility to obtain the instrumental contribution to the visibility, called here simply the instrument visibility.

Because the measured visibility involves the mean value as well as the fringe amplitude, it is particularly susceptible to contamination by stray light, and tests were designed to distinguish stray light effects. Theoretical analyses[30] of filter-reflected light and CCD-reflected light had shown that the mean value could be contaminated and that the fringe shape could become nonsinusoidal through the superposition of double-frequency fringes. Both effects reduce the measured visibility. Tests were performed with no filter, with a filter at normal incidence, and with a filter tilted by an angle corresponding to one-half the field of view, and the instrument visibilities determined are shown in Table II. The visibilities of the instrument with no filter and with a tilted filter are the same. For the filter normal to the optical axis the instrument visibility is reduced. For increasing wavelength the instrument visibility increases, as expected from the decreasing fractional wave front error. The CCD reflectance is less than that of the interference filter and a much smaller visibility reduction effect was found for the CCD. (This was determined by comparing the visibility for on-axis pixels with those farthest from the axis.)

The detailed measurement of the fringe shape carried out in the step size calibration revealed a double-frequency fringe superposed on the main fringe. Such fringes had been predicted[30] for filter-reflected light but these fringes were observed even without a filter. This unexpected result appears to be caused by the poor performance of the LaF21 antireflection coating, which possibly was degraded by outgassing from the RTV cushion used to support the optics. This causes a weak (~2%) reflection directly from the end of the arm, and an additional reflection of mirror-reflected light off the end of the arm and back to the mirror again. The first reflection gives stationary fringes corresponding to the thin vacuum gap, while the second reflection gives rise to scanning fringes that have twice the frequency of the main fringes. Although these fringes were only a few percent of the main fringes they were clearly evident in the data, and it was necessary to remove them by data processing.

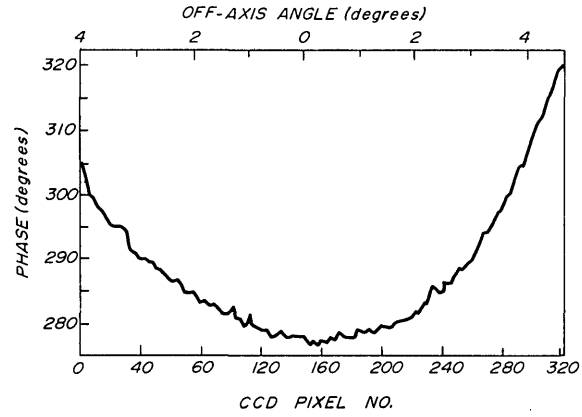

Fig. 9. Phase shift vs off-axis angle plotted as pixel number for one row of the CCD. The corresponding off-axis angles are also shown.

D. Field Wideness and Achromaticity

The use of an imaging detector simplified the generation of field-wideness curves. The calculated phase was plotted for the CCD row passing through the minimum phase pixel for the entire image, and the result for 650.65 nm is shown in Fig. 9. The horizontal axis corresponds to off-axis angles of 4.0° on the left, and 4.6° on the right. The phase shift at 4.0° is ~28°, corresponding to 0.08 wavelengths, and this is substantially larger than the predicted value shown in Fig. 2. The irregularity of the curve is due primarily to individual inferior pixels present on the setup quality CCD used for these tests.

Field-wideness curves were generated for a number of wavelengths covering the range of interest in order to assess the chromatic compensation. The field wideness was slightly worse than the predicted values, generally elevating the curves of Fig. 2. It was concluded that the differences between the measured and predicted characteristics arose from limitations in the accuracy of the glass constants used. The field wideness achieved is fully acceptable for the flight instrument, and amounts to only λ/400 across a single pixel.

Table III. Accuracy of the Phase Calibration (In Degrees)

Actual wavelength \ Calibration wavelength		585.249	692.947	724.517
Temperature Shift: 2.55°C	585.249	*	−0.714	−0.377
	650.653	0.505	−0.137	0.166
	692.947	0.603	*	0.285
	717.394	−0.105	−0.688	−0.413
	724.517	0.304	−0.272	*
Temperature Shift: 1.35°C	585.249	*	−0.200	−0.241
	650.653	−0.019	−0.199	−0.236
	692.947	0.169	*	−0.035
	717.394	0.461	0.298	0.264
	724.517	0.195	0.033	*

E. Thermal Compensation

The thermal compensation of the MI was evaluated experimentally by measuring the phase of the emission line source at several wavelengths with the MI enclosure stabilized at several temperatures from 23.53°C to 26.08°C. The phase was found to decrease by 40° for each 1°C of temperature increase and was almost independent of the wavelength. Again this was attributed to errors in the knowledge of α and dn/dT, these values having been simply taken from the glass catalog.

F. Phase Calibration

To determine absolute wind velocity during the flight, the phase of the atmospheric emission corresponding to zero velocity must be derived. Since an atmospheric emission line source cannot be launched with the instrument, the phase must be calibrated indirectly. The phase of the in-flight atmospheric emission corresponding to zero velocity will be predicted by measuring the phase of one or more emissions from an onboard calibration source and by knowledge of the relationship between the phase of the atmospheric emissions and the phase of the calibration source emission lines as determined from ground measurements.

The accuracy of the phase calibration algorithm was evaluated by predicting the phase at certain wavelengths using other wavelengths as the standard and subtracting the actual phase measured at the same wavelength from the predicted one. Two MI temperature shifts were considered, 2.55°C and 1.35°C, corresponding to variations much larger than are expected in flight. These phase prediction errors are shown in Table III for different combinations of actual and calibration wavelengths (the * indicates the standard wavelength). It may be seen that the phase was always predicted to better than 1°, corresponding to a velocity error of <10 m/sec.

The phase shift corresponding to the temperature change is very uniform across the entire CCD array. This indicates that the shape of the field-wideness curves remains the same for different temperatures.

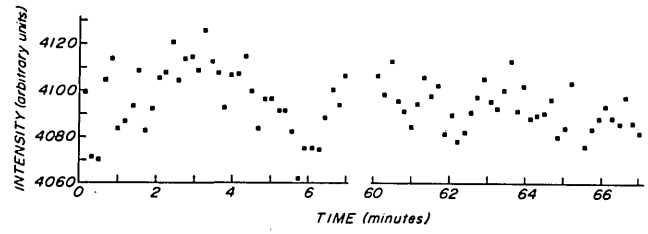

Fig. 10. Stability test showing measured intensity for a fixed mirror position over two 7-min periods separated by 1 h.

G. Thermal Stability

The thermal stability requirements described in Sec. III.D are achieved by actively controlling an outer thermal enclosure (OTE) with heaters and a thermoelectric cooler. The OTE is radiatively coupled to an isothermal inner thermal enclosure (ITE) containing the MI, all as shown in Fig. 8. The performance of the thermal control system was measured in the laboratory tests, in field tests, and in thermal/vacuum tests. The MI temperature, as monitored by the phase data, was shown to be decoupled from the environment exterior to the OTE for an environmental temperature range from −12°C to 30°C in vacuum. Undersized thermoelectric coolers and small heat leaks limited this value to 30°C rather than the design value of 50°C. The objective will be achieved in the flight instrument by appropriate redesign.

H. System Stability

To achieve the required wind and temperature accuracy, a high degree of stability is required in many of the instrument subsystems. To evaluate the overall stability the position of the scanning mirror was set to the phase corresponding to the maximum slope of the interferogram for the source used. Forty images were recorded at this fixed mirror position over a period of 7 min. The same sequence was repeated 1 h later. The detector response was plotted vs time as shown in Fig. 10. It is evident that the data points are evenly distributed with an overall system error of ±0.5%. It should be emphasized that this tests involves the stabilities of the following components: the emission line source, the mirror position controller, the MI temperature controller, the CCD thermal controller, and the exposure time controller. The high stability of individual subsystems was confirmed at various stages of the WAMDII testing. Typical variations of CCD temperature were ±0.02°C peak-to-peak. The exposure time is computer controlled with an accuracy of ±10-msec peak-to-peak, corresponding to ±0.1% in the case of a typical exposure of 10 sec.

I. Summary

The results of the laboratory tests can be summarized as follows:

(1) The MI field wideness is acceptably achromatic from 546 to 764 nm.

(2) The MI temperature coefficient is approximately −40° of phase/°C.

(3) The MI visibility is 0.80–0.90, increasing with increasing wavelength.

(4) The capacitive feedback piezoelectrically scanned mirror assembly is reliable and repeatable to better than $\lambda/500$.

(5) The concept of thermal control of the MI to better than 0.01°C has been confirmed.

(6) The overall system stability is better than ±0.5%.

(7) Phase calibration to better than 1° of phase across the WAMDII spectral region has been confirmed.

(8) The suitability of a CCD as a highly precise photometric detector for the WAMDII has been confirmed.

VIII. Field Test Results

In February 1984, the WAMDII was moved to a field site maintained by the University of Saskatchewan, 27 km west of Saskatoon. During a two-week observing period, about 2500 sets of images of the night sky were obtained at the oxygen emission wavelengths of 557.7 and 630.0 nm. Aurora was present most clear nights and, on a few occasions, very active displays were seen. The purpose of the tests was to study the capabilities of the instrument in real observing conditions. A set of foreoptics was installed which expanded the field of view in the sky to 12° × 16°. Large (10-cm square) interference filters with bandwidths of ~1 nm were obtained from Barr Associates for the two oxygen wavelengths and these were installed on slides just in front of the beam splitter. Two smaller filters for measuring background intensities were mounted on a slide ahead of the foreoptics. In addition, a 45° mirror permitted observation of the emission line calibration source.

The WAMDII was located indoors and looked out through a small window into a large, plane mirror set at 45° to a rotation axis which allowed the field of view to be moved along a north–south meridian.

During observations, the phase of the fringes was found to be very stable and phase calibrations were done only about once an hour. In all cases, a set of images consisted of four exposures spaced $\lambda/4$ apart in path difference. Exposure times ranged from 1 to 10 sec, depending on the source brightness. Observing time was approximately equally divided between the red and green emissions. Airglow was observed as well as aurora, ranging from bright, active displays to faint, stable arcs and glows. As no laboratory source of the OI emissions was available, observations made in the zenith were assumed to represent zero wind. Phase images taken in other directions were referenced to the zenith observations via the regular phase calibrations.

Information generated by the WAMDII was stored in digital format on half-inch magnetic tape for subsequent off-line processing. This information is of two types: the interferogram point measurements for each interferometer (pixel) and auxiliary data relating to such things as the time and location of the measurement as well as the orientation of the instrument and its operating environment. The main objective of the off-line data processing is to produce physically meaningful estimates of the atmospheric quantities of emission rate, temperature, and wind.

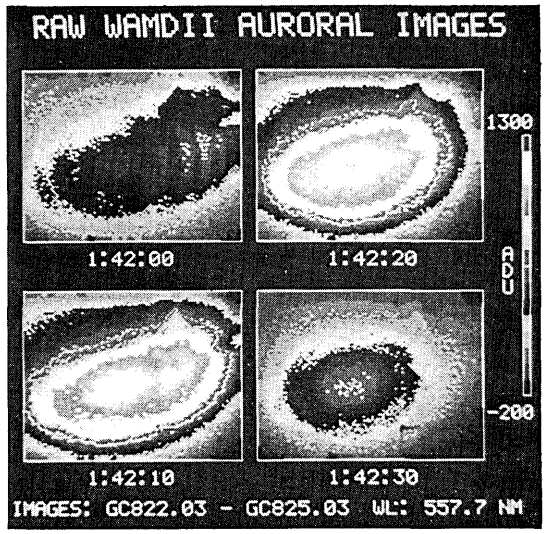

Fig. 11. Scene comprising four successive images of an auroral arc with 90° phase steps between each image.

The interferogram point measurements are organized in terms of images and scenes. An image is a double sequence $\{I(j,k,t)\}$ where the time of measurement, specified by the integer t, is fixed and the integers j and k define the interferometer or its corresponding CCD element. A scene consists of a sequence of images, defined by successive values of t which in turn specify phase or path differences for each interferometer with the restriction that the phase cannot change more than 2π rad. As indicated by Eqs. (8)–(11), four successive images generally constitute a scene. From each scene an emission rate, temperature, and wind component velocity may be evaluated as functions of time and two spatial coordinates relating to the location of the locally stationary atmospheric emission under study.

The information contained in each image must be corrected for intensity and phase in an absolute sense and estimated values of the mean dark current and readout noise must be removed. Other known instrumental corrections are made at this time. The corrected images in a scene may then be combined to calculate the three atmospheric parameters.

In Fig. 11 a scene is presented comprising four images of an auroral arc, each of 10-sec exposure, but with a 90° phase shift between successive images. For these (inverted) 557.7-nm images the field of view was positioned 30° above the northern horizon; the attenuation at the edges of the arc results from the reduced transmission of the interference filter at large off-axis angles. The steps in processing of a phase image are shown in Fig. 12. The auroral phase image (upper left) is computed pixel by pixel, using Eq. (14). The lamp phase is calculated in the same manner, using four images obtained from a spectral lamp source emission line at 585.5 nm. The wind phase (lower left) is the difference between

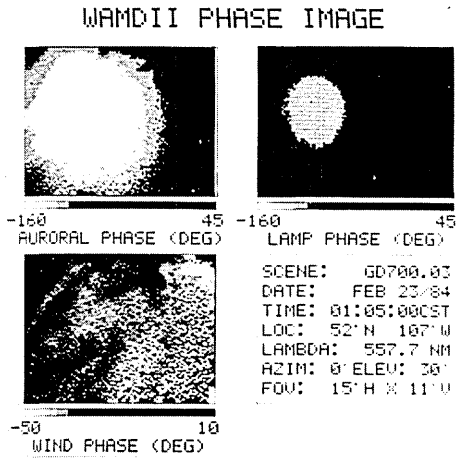

Fig. 12. Phase images of the aurora computed from Fig. 11 of a spectral lamp and of the difference which yields the true wind phase.

the first two images. It is essentially a velocity image in m/sec if one multiplies the scale in degrees by 10. Considerable structure is evident in this image, in particular in the upper left corner where linear wave structures can be seen, having a vertical wavelength of 10 km. This wave event has been described in more detail elsewhere.[31]

IX. Comparison with Other Optical Doppler Methods

The optical Doppler method for the measurement of upper atmospheric winds and temperatures has been firmly established for the Fabry-Perot spectrometer. Major contributors to this have been Hernandez and Roble,[32] Hays *et al.*,[33] Rees *et al.*,[34] Smith *et al.*,[35] Sipler *et al.*[36] for ground-based observations, and Hays *et al.*[37] for satellite observations. It is not possible to review the full scope of this work in this brief section, and the comparison shall be restricted to a few specific systems that involve imaging.

Sivjee *et al.*[38] describe a "Fabry-Perot-interferometer imaging system" that employs a low-light level image-orthicon TV camera coupled to a two-stage image intensifier. The image is analyzed for spectral information by averaging the data into FPS rings, greatly decreasing the time required to obtain a spectrum. This technique really amounts to field widening a FPS for the purpose of enhancing the responsivity of measurement for a single source point on the sky. Hays[39] describes a "High Resolution Doppler Imager Interferometer System" that employs three F.P. etalons and an image plane detector. This powerful system has a unique passband that may be applied to absorption lines or emission lines of any shape, but again the multielement detector is used to explore the spectrum, and the imaging of the source is accomplished by raster scanning the field of view.

Rees *et al.*[34] describe a Doppler imaging system (DIS) that uses an IPD (imaging photon detector) and all sky optics that image the fringes on the sky. The etalon is of fixed spacing, so that the image is analyzed for both spatial and spectral information. The spatial resolution is then determined by the number of rings located on the sky, and the spectral resolution by the number of pixels devoted to a single ring. It is also necessary to assume that spatial and spectral information are separable. The WAMDII resembles the DIS more than any of the other systems described above, but there are still important differences. Because the WAMDII mirror is stepped, all pixels yield wind and temperature values, and there is no need to assume that spatial information and spectral information are separable over the image; rather one can assume that they are independent. This capability is not essential for ground-based measurements, but it is crucial for limb observations from space.

We have consistently referred to the Fabry-Perot device as a spectrometer, since functionally it operates by exploring the spectrum with a scanning filter—as do all spectrometers. The MI is referred to as an interferometer because its output is an interferogram, the Fourier transform of the spectrum. However, for the method used here, the difference is less fundamental. There is an implied correspondence principle that states that a FPS of low finesse corresponds to a MI (in fact if there were only two beams emerging from the FPS cavity the instruments would be identical). For wind measurements, the FPS and WAMDII both measure fringe shifts in very much the same way. For temperature measurements there is more difference. The FPS detects changes in fringe shape as temperature changes, while the WAMDII detects changes in modulation depth. Put differently, the WAMDII relies on highly precise knowledge of its sinusoidal instrumental passband to interpret visibility changes as temperature while the FPS relies on accurate measurement of line shapes, based on accurate determination of the instrumental passband shape from calibration sources. The FPS places weaker requirements on the nature of the source but requires more measurements per fringe. For a FPS optimized for winds, Hernandez[40] has shown that the minimum number of samples per fringe is approximately four times the finesse and describes one case where 8 points is an optimum number. Compared to the number four used for the WAMDII, this configuration represents the closest correspondence of the two classes of instrument.

While apart from the references cited earlier, this is the first application of a field-widened MI to studies in aeronomy, it has already been applied by solar physicists to the problem of solar velocity fields.[41–43] The concept could well be applicable to a number of other areas.

X. Conclusions

A field-widened Michelson interferometer has been described in an achromatic configuration that is reasonably insensitive to temperature changes. With a CCD imaging detector and a mirror stepper that permits accurate quarterwave steps, four images may be acquired that can be converted to images of temperature, velocity, intensity, and intensity change. However, it is necessary to restrict the source to single Gaussian emission line profiles using a prefilter.

The laboratory measurements show that the field widening is achromatic from 557 to 760 nm, and the temperature coefficient is ~45° of phase/°C. The field measurements show that useful images of low intensity aurora can be obtained in exposures of 10 sec. More detailed analysis shows that a 1-kR emission rate requires exposure times of 5 sec to obtain winds with an error of 10 m/sec.

In comparison with existing FPS instrumentation the WAMDII compares most closely with a stepped FPS with an imaging detector, but there are three important differences:

(1) The FPS senses line shape while the MI senses modulation depth.

(2) The off-axis angle in both instruments is limited by the phase change across a single pixel; this is more restrictive for the FPS which is not inherently field widened (the DIS works to an angle of 2° while the WAMDII operates to ~8°).

(3) The MI acquires data more efficiently, requiring only four images per measurement.

A full description of the WAMDII instrument involves a description of the foreoptics, the control of reflections within the system, the thermal control method, as well as the CCD camera and the design of electronic subsystems. These will be described at the completion of the next phase of the work.

The WAMDII Spacelab instrument development and fabrication is supported by the Canada Centre for Space Science, National Research Council, while the scientific aspects of instrument specification and data analysis are supported by the Natural Sciences and Engineering Research Council. The prime contractor is SED Systems, Inc., Saskatoon. The present stage has been reached with the help of many individuals; we acknowledge particularly the support of R. Wlochowicz, the NRC project manager, and K. L. Krukewich, the SED project manager. The WAMDII concept depends heavily on the Queensgate Instruments, London, mirror controller, and we thank T. Hicks for his support. The WAMDII coinvestigator team comprises G. G. Shepherd (principal investigator), R. A. Koehler and J. C. McConnell of York University; C. D. Anger, L. L. Cogger, and J. W. Haslett of the University of Calgary; E. J. Llewellyn and K. V. Paulson of the University of Saskatchewan; D. R. Moorcroft of the University of Western Ontario and R. L. Gattinger of the Herzberg Institute of Astrophysics, NRC.

References

1. G. Hansen, "Die Sichtbarkeit der Interferenzen beim Twyman-Interferometer," Optik **12,** 5 (1955).
2. G. Hansen and W. Kinder, "Abhängigkeit des kontrastes der Fizeau-Streifen im Michelson-Interferometer vom Durchmesser der Aperturblende," Optik **15,** 560 (1958).
3. J. W. Evans, "The Birefringent Filter," J. Opt. Soc. Am. **39,** 229 (1949).
4. L. Mertz, "A Fourier Description of Optical Interference Devices Part I," J. Opt. Soc. Am. **49,** iv (1959).
5. L. Mertz, *Transformations in Optics* (Wiley, New York, 1965).
6. L. Mertz, "Field Widened Michelson Interferometer," J. Opt. Soc. Am. **57,** No. 2, iv (1967).
7. P. Bouchareine and P. Connes, "Interféromètre a Champ Compensé Pour Spectroscopie par Transformation de Fourier," J. Phys. Radium **24,** 134 (1963).
8. W. H. Steel, *Interferometry* (Cambridge U.P., London, 1967).
9. D. Baker, "Field-Widened Interferometers for Fourier Spectroscopy," in *Spectrometric Techniques, Vol. 1,* G. Vanasse, Ed. (Academic, New York, 1977).
10. R. L. Hilliard and G. G. Shepherd, "Wide-Angle Michelson Interferometer for Measuring Doppler Line Widths," J. Opt. Soc. Am. **56,** 362 (1966).
11. J. Ring and J. W. Schofield, "Field Compensated Michelson Spectrometers," Appl. Opt. **11,** 507 (1972).
12. D. Baker, A. Steed, and A. T. Stair, Jr., "Development of Infrared Interferometry for Upper Atmospheric Emission Studies," Appl. Opt. **20,** 1734 (1981).
13. R. L. Hilliard and G. G. Shepherd, "Upper Atmospheric Temperature from Doppler Line Widths," Planet. Space Sci. **14,** 383 (1966).
14. H. H. Zwick and G. G. Shepherd, "Auroral Electron Energy Spectra and Fluxes Deduced From the 5577 and 6300Å Atomic Oxygen Emissions," Planet. Space Sci. **21,** 605 (1973).
15. G. G. Shepherd, C. W. Lake, J. R. Miller, and L. L. Cogger, "A Spatial Spectral Scanning Technique for the Fabry-Perot Spectrometer," Appl. Opt. **4,** 267 (1965).
16. J. Katzenstein, "The Axicon-Scanned Fabry-Perot Spectrometer," Appl. Opt. **4,** 263 (1965).
17. T. L. Killeen, B. C. Kennedy, P. B. Hays, D. A. Symanow, and D. H. Ceckowski, "Image Plane Detector for the Dynamics Explorer Fabry-Perot Interferometer," Appl. Opt. **22,** 3503 (1983).
18. W. A. Gault and G. G. Shepherd, "WAMDII—A Wide Angle Michelson Doppler Imaging Interferometer for Spacelab," Adv. Space Res. **2,** 111 (1983).
19. D. J. W. Kendall, S. F. Johnston, J. A. Dobrowolski, and G. G. Shepherd, "A Polarizing Wide-Angle Michelson Interferometer for Doppler Measurements of Atmospheric Emissions," paper 54 presented at 1983 International Conference on Fourier Transform Spectroscopy, Durham, England (Sept. 1983).
20. T. L. Killeen and P. B. Hays, "O('S) From Dissociative Recombination of O_2^+: Nonthermal Line Profile Measurements From Dynamics Explorer," J. Geophys. Res. **88,** 10163 (1983).
21. A. M. Title and H. E. Ramsey, "Improvements in Birefringent Filters. 6: Analog Birefringent Elements," Appl. Opt. **19,** 2046 (1980).
22. H. H. Zwick and G. G. Shepherd, "Defocusing a Wide-Angle Michelson Interferometer," Appl. Opt. **10,** 2569 (1971).
23. F. Landauer, J. R. Janesick, S. L. Knapp, M. M. Blouke, and J. R. Hall, "An 800 × 800 CCD Imager for Space-Borne Scientific Imaging," Jet Propulsion Laboratory, California Institute of Technology (1979).
24. D. F. Barbe, "Noise and Distortion Considerations in Charge-Coupled Devices," Electron. Lett. **8,** 207 (1972).
25. D. F. Barbe, "Imaging Devices Using the Charge-Coupled Concept," Proc. IEEE **63,** 38 (1975).
26. A. Fowler, P. Waddell, and L. Mortara, "Evaluation of the RCA 512 × 320 Charge-Coupled Device Imagers for Astronomical Use," Proc. Soc. Photo-Opt. Instrum. Eng. **290,** 34 (1981).
27. J. A. Dobrowolski, F. C. Ho, and A. Waldorf, "Beam Splitter for a Wide Angle Michelson Doppler Imaging Interferometer," Appl. Opt. **24,** (1985), this issue.
28. T. R. Hicks, N. K. Reay, and R. J. Scaddan, "A Servo Controlled Fabry-Perot Interferometer Using Capacitance Micrometers for Error Detection," J. Phys. E **7,** 27 (1974).
29. J. R. Wimperis and S. F. Johnston, "Optical Cements for Interferometric Applications," Appl. Opt. **23,** 1145 (1984).

30. W. E. Ward, Z. Pasturczyk, W. A. Gault, and G. G. Shepherd, "Multiple Reflections in a Wide Angle Michelson Interferometer," Appl. Opt. **24,** (1985), this issue.
31. G. G. Shepherd *et al.*, "Optical Doppler Imaging of the Aurora Borealis," Geophys. Res. Lett. **11,** 1003 (1984).
32. G. Hernandez and R. G. Roble, "Thermospheric Dynamics Investigations with Very High Resolution Spectrometers," Appl. Opt. **18,** 3376 (1979).
33. P. B. Hays, J. W. Meriwether, and R. G. Roble, "Nighttime Thermospheric Winds at High Latitudes," J. Geophys. Res. **84,** 1905 (1979).
34. D. Rees, A. H. Greenaway, R. Gordon, I. McWhirter, P. J. Charleton, and A. Steen, "The Doppler Imaging System: Initial Observations of the Auroral Thermosphere," Planet. Space Sci. **32,** 273 (1984).
35. R. W. Smith, K. Henriksen, C. S. Deehr, D. Rees, F. G. McCormac, and G. G. Sivjee, "Thermospheric Winds in the Cospia Dependence of the Latitude of the Cusp," Planet. Space Sci. **33,** 305 (1985).
36. D. P. Sipler, M. A. Biondi, and R. G. Roble, "F-Region Neutral Winds and Temperatures at Equatorial Latitudes: Measured and Predicted Behaviour During Geomagnetically Quiet Conditions," Planet. Space Sci. **31,** 53 (1983).
37. P. B. Hays *et al.*, "Observations of the Dynamics of the Polar Thermosphere," J. Geophys. Res. **89,** 5597 (1984).
38. G. G. Sivjee, T. J. Hallinan, and G. R. Swenson, "Fabry-Perot-Interferometer Imaging System for Thermospheric Temperature and Wind Measurements," Appl. Opt. **19,** 2206 (1980).
39. P. B. Hays, "High-Resolution Optical Measurements of Atmospheric Winds from Space. 1: Lower Atmosphere Molecular Absorption," Appl. Opt. **21,** 1136 (1982).
40. G. Hernandez, "Analytical Description of a Fabry-Perot Spectrometer. 6: Minimum Number of Samples Required in the Determination of Doppler Widths and Shifts," Appl. Opt. **21,** 1695 (1982).
41. T. M. Brown, "The Fourier Tachometer: Principles of Operation and Current Status," in *Solar Instrumentation: What's Next?, Proceedings, Sacramento Peak National Observatory Conference* (1982), p. 150.
42. J. W. Evans, "The Fourier Tachometer: The Solid Polarizing Interferometer," in *Solar Instrumentation: What's Next?, Proceedings, Sacramento Peak National Observatory Conference* (1982), p. 155.
43. J. O. Stenflo, "Solar Magnetic and Velocity-Field Measurements: New Instrument Concepts," Appl. Opt. **23,** 1267 (1984).

Meetings Calendar *continued from page 1570*

1985
June

10–14 Introduction to Techniques For Information Extraction From Remotely Sensed Data course, Wash., D.C. *P. Vidal, Geo. Wash. U., Cont. Eng. Ed., Wash., D.C. 20052*

10–14 Fundamentals & Applications of Lasers course, Wash., D.C. *Laser Inst. of Amer., 5151 Monroe St., Toledo, Ohio 43623*

10–14 Laser Safety: Hazard, Inspection & Control course, Wash., D.C. *Laser Inst. of Amer., 5151 Monroe St., Toledo, Ohio 43623*

11–14 Image Science & Technology ICO Conf., Helsinki *P. Oittinen, Helsinki U. Technology, Lab. of Graphic Arts Tech., Tekniikantie 3, 02150 Espoo 15, Finland*

12–14 **Workshop on Optical Fabrication & Testing, OSA Tech. Mtg.,** Cherry Hill *OSA Mtgs. Dept, 1816 Jefferson Pl., N.W., Wash., D.C. 20036*

17–18 Laser Nurse Seminar & Workshop, Chicago *Laser Inst. of Amer., 5151 Monroe St., Toledo, Ohio 43623*

17–19 43rd Ann. Device Research Conf., Boulder *L. Tomasetta, Vitesse Electronics, 741 Calle Plano, Camarillo, Calif. 93010*

17–19 Int. Conf. on Chemical Kinetics, Gaithersburg *J. Herron, A147 Chem. Bldg., NBS, Wash., D.C. 20234*

17–21 Database Management Using Personal Computers course, Ann Arbor *Eng. Summer Confs., 200 Chrysler Ctr., N. Campus, U. of Mich., Ann Arbor, Mich. 48109*

17–21 Infrared Technology Fundamentals & System Applications course, Ann Arbor *Eng. Summer Confs., 200 Chrysler Ctr., N. Campus, U. of Mich., Ann Arbor, Mich. 48109*

18–21 Instabilities & Dynamics of Lasers & Nonlinear Optical Systems Mtg., Rochester *OSA Mtgs. Dept., 1816 Jefferson Pl., N.W., Wash., D.C. 20036*

19–21 Local Area Networks course, Detroit *Data-Tech Inst., Lakeview Plaza, P.O. Box 2429, Clifton, N.J. 07015*

23–30 Soc. of Women Engineers Ann. Natl. Convention, Minneapolis *G. Hinschberger, P.O. Box 9542, Minneapolis, Minn. 55440*

24–28 7th Int. Conf. on Laser Spectroscopy, Maui *T. Hansch, Physics Dept., Stanford U., Stanford, Calif. 94305*

24–28 Int. Conf. on Fourier & Computerized Infrared Spectroscopy, Ottawa *L. Baignee, Conf. Services Office, Ottawa, Ontario KIA OR6, Canada*

24–28 Robotics: Concepts, Theory & Applications course, Ann Arbor *Eng. Summer Confs., 200 Chrysler Ctr., N. Campus, U. of Mich., Ann Arbor, Mich. 48109*

24–28 Advanced Infrared Technology course, Ann Arbor *Eng. Summer Confs., 200 Chrysler Ctr., N. Campus, U. of Mich., Ann Arbor, Mich. 48109*

continued on page 1643